
DeepLag: Discovering Deep Lagrangian Dynamics for Intuitive Fluid Prediction

Qilong Ma,* Haixu Wu,* Lanxiang Xing, Shangchen Miao, Mingsheng Long[✉]

School of Software, BNRist, Tsinghua University, China

{mq122, wuhx23, xlx22, msc21}@mails.tsinghua.edu.cn, {mingsheng}@tsinghua.edu.cn

Abstract

Accurately predicting the future fluid is vital to extensive areas such as meteorology, oceanology, and aerodynamics. However, since the fluid is usually observed from an Eulerian perspective, its moving and intricate dynamics are seriously obscured and confounded in static grids, bringing thorny challenges to the prediction. This paper introduces a new Lagrangian-Eulerian combined paradigm to tackle the tanglesome fluid dynamics. Instead of solely predicting the future based on Eulerian observations, we propose DeepLag to discover hidden Lagrangian dynamics within the fluid by tracking the movements of adaptively sampled key particles. DeepLag utilizes the proposed where the Lagrangian movement of the tracked particles is inferred from Eulerian observations, and their accumulated Lagrangian dynamics information is incorporated into global Eulerian evolving features to guide future prediction respectively. Tracking key particles not only provides a transparent and interpretable clue for fluid dynamics but also makes our model free from modeling complex correlations among massive grids for better efficiency. Experimentally, DeepLag excels in three challenging fluid prediction tasks covering 2D and 3D, simulated and real-world fluids.

1 Introduction

Fluids, characterized by a molecular structure devoid of resistance to external shear forces, readily undergo deformation even under minimal force, thereby typically presenting extremely complex dynamics [10]. Consequently, the solvability of theorems for fluid mechanics, such as Navier-Stokes equations, is confined to a limited subset of flows due to the complex form and intricate multiphysics interactions [38]. In practical applications, computational fluid dynamics (CFD) is widely used to infer future fluid by numerical simulations. However, it suffers from substantial computation costs due to the curse of dimensionality [40]. Till now, accurately predicting future dynamics is still a challenging problem. Recently, benefiting from the tremendous non-linear modeling capability, deep models [8, 28, 22] have emerged as a promising tool for fluid prediction, which can be trained with CFD simulations or real-world observations and perform as a fast surrogate model during inference.

A booming direction for deep fluid prediction is learning deep models to solve governing partial differential equations (PDEs) [45]. However, most of these methods [48, 29, 22, 21] attempt to capture fluid dynamics from the Eulerian perspective, which means modeling spatiotemporal correlations among massive grids remains unchanged over time. From this perspective, the complicated moving dynamics in fluids could be seriously obscured and confounded in static grids, bringing challenges in both computational efficiency and learning difficulties in accurately predicting future fluids.

Apart from the Eulerian method, we notice another approach for elucidating fluid dynamics, the Lagrangian method [13], also known as the tracking method. This method primarily focuses on tracing

* Equal Contribution

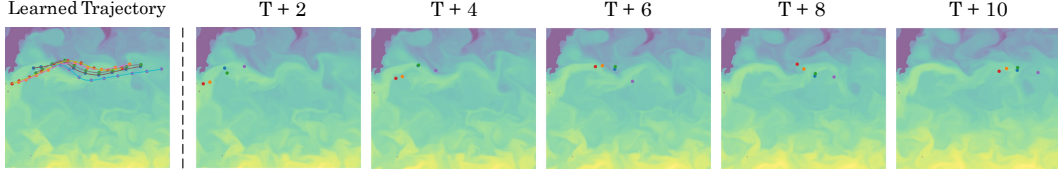


Figure 1: Comparison between Lagrangian and Eulerian perspectives. The left part presents the trajectory of five representative particles learned by DeepLag in the Ocean Current dataset, which provides a Lagrangian perspective for Eulerian-recorded fluid on the right.

individual fluid particles by conducting the temporal evolution of the position and velocity of each particle. Unlike the Eulerian methods, the Lagrangian approach describes the fluid dynamics through the moving trajectory of individual fluid particles, offering a more natural and neat representation of fluid dynamics with inherent advantages in capturing intricate flow dynamics. Moreover, it helps get around the Courant–Friedrichs–Lowy condition [6] for advection, allowing larger timesteps while retaining stability. As shown in Figure 1, we can find that fluid dynamics is much more apparent in the Lagrangian trajectory than the density change on static Eulerian grids.

Building on the two perspectives mentioned earlier, we propose DeepLag as an Eulerian-Lagrangian Recurrent Network. Our aim is to integrate Lagrangian tracking into the deep model, thereby enhancing the dynamics modeling in Eulerian fluid prediction. To achieve this, we present the EuLag Block, a powerful tool that accomplishes Lagrangian tracking and Eulerian predicting at various scales. By leveraging the cross-attention mechanism, the EuLag Block assimilates tracked Lagrangian particle dynamics into the Eulerian field, guiding fluid prediction. It also forecasts the trajectory and dynamics of Lagrangian particles with the aid of Eulerian features. This unique Eulerian-Lagrangian design harnesses the dynamics information captured by Lagrangian trajectories and the fluid-structure feature learned in the Eulerian grid. In our experiments, DeepLag consistently outperforms existing models, demonstrating its state-of-the-art performance across three representative datasets, covering 2D and 3D fluid at various scales. Our contributions are as follows:

- Going beyond learning fluid dynamics at static grids, we propose DeepLag featuring the Eulerian-Lagrangian Recurrent Network, which is the first deep fluid prediction model that explicitly combines Eulerian and Lagrangian frameworks from fluid dynamics concisely.
- Inspired by Lagrangian mechanics, we present EuLag Block, which can accurately track particle movements and interactively utilize the Eulerian feature and dynamic information in fluid prediction, enabling a better dynamic modeling paradigm.
- DeepLag achieves consistent state-of-the art on three representative fluid prediction datasets with superior trade-offs for performance and efficiency, exhibiting favorable practicability.

2 Preliminaries

2.1 Eulerian and Lagrangian methods

Eulerian and Lagrangian descriptions are two fundamental perspectives for describing fluid motion. The Eulerian view, commonly used in practical applications [23], observes fluid at fixed points and records physical quantities, such as density, as a function of position and time, $\mathbf{v} = \mathbf{v}(\mathbf{s}, t)$. Thus, future fluid can be predicted by integrating velocity along the temporal dimension and interpolating results to observed grid points [49]. In contrast, the Lagrangian perspective focuses on the trajectory of individual particles, tracking a particular particle with initial position \mathbf{s}_0 with its displacement $\mathbf{d} = \mathbf{d}(\mathbf{s}_0, t)$ at time t . This approach reveals the intricate evolution of the fluid by following particle trajectories, making it convenient for describing complex phenomena like vortices, turbulence, and interface motions [39]. Two perspectives are constitutionally equivalent, as bridged by the velocity:

$$\mathbf{v}(\mathbf{d}(\mathbf{s}_0, t), t) = \frac{\partial \mathbf{d}}{\partial t}(\mathbf{s}_0, t). \quad (1)$$

Furthermore, the material derivative that describes the change rate of a physical quantity q of a fluid parcel can be written as the sum of the two terms reflecting the spatial and temporal influence on

\mathbf{q} [1], which represent the derivatives on Eulerian domain and Lagrangian convective respectively:

$$\frac{D\mathbf{q}}{Dt} = \underbrace{\frac{\partial \mathbf{q}}{\partial t}}_{\text{domain derivative}} + \underbrace{\mathbf{u} \cdot \nabla \mathbf{q}}_{\text{convective derivative}}. \quad (2)$$

This connection inspires us to incorporate Lagrangian descriptions into dynamics learning with Eulerian data, enabling a more straightforward decomposition of complex spatiotemporal dependencies.

While traditional particle-based (or mixed-representation) solvers demonstrate superior accuracy and adaptability in inferring small-scale phenomena and dealing with nonlinear and irregular boundary conditions, they require computing the acceleration of each particle through physical equations, followed by sequential updates of their velocity and position [31]. This pointwise modeling approach often demands a significant number of points to fully characterize the dynamics of the entire field to meet accuracy requirements. Moreover, the irregular arrangement of particles and difficulty in parallelization result in higher computational costs and challenges with particle interpolation and gridding [12]. This renders particle-based solvers suboptimal compared to Eulerian solvers, particularly in high-dimensional spaces and large-scale simulations. However, DeepLag leverages the strengths of both solvers, eschewing equations and instead utilizing Eulerian information to assist particle tracking directly. This greatly alleviates the pressure on Lagrangian representation, requiring significantly fewer representative particles to aggregate the dynamics of the entire field.

2.2 Neural Fluid Prediction

Since traditional CFD methods often require hours or even days for precise simulations [41], deep models have been widely explored as efficient surrogate models that can provide near-instantaneous predictions. These neural fluid prediction models approximate the solutions of governing fluid equations differently and can be categorized into three mainstream paradigms as in Figure 2(a-c).

ODE-based Generative Models As depicted in Figure 2(a), these methods [4, 26, 55] encode multivariate fields into a single-variable latent state \mathbf{z} , on which they model an ODE governing the state function $\mathbf{z}_t : \mathcal{T} \rightarrow \mathbb{R}^d$, representing the first-order time derivative, through neural networks. However, the absence of physical meaning and guidance for latent states in evolution leads to error accumulation and a generally short forecasting horizon. A detailed comparison between DeepLag and these models is provided in Appendix B.

Neural PDE Solvers This branch of methods in Figure 2(b) adopts deep models to learn the mapping from coordinates to correct values and formalize PDE constraints along with initial and boundary conditions as the loss function of deep models [48, 29, 46, 47]. Though this paradigm can precisely approximate the PDE solution, they usually require exact formalization for coefficients and conditions, limiting their generality and applicability to real-world fluids that are usually partially observed [35]. Plus, the Eulerian input disables them from handling Lagrangian descriptions.

Neural Operators for PDE Recently, a new paradigm, illustrated in Figure 2(c), has emerged where deep models learn the neural operators between input and target functions, e.g., past observations to future fluid predictions. Various neural operators have significantly advanced fluid prediction following the DeepONet [22], which directly approximates mappings between equation parameters and solutions. For Eulerian grid data, models based on U-Net [32] and ResNet [15] structures have been proposed [30, 27, 17], as well as variants addressing issues like generalizing to unseen domains [44], irregular mesh [11], and uncertainty quantification [51]. Transformer-based models [43] enhance modeling capabilities and efficiency by exploiting techniques like Galerkin attention [3], incorporating ensemble information from the grid [14], applying low-rank decomposition to the attention mechanism [20], and leveraging spectral methods in the latent space [52]. Additionally, FNO [21] learns mappings in the frequency domain, and MP-PDE [2] utilizes the message-passing mechanism. For Lagrangian fluid particle data, some CNN-based methods [34, 42] model particle interactions through redesigned basic modules, while GNN-based methods [33, 25] update particle positions using the Encode-Process-Decode paradigm. Despite the progress made by these methods, they are limited to one description and do not organically combine both perspectives.

3 DeepLag

Following the convention [21], we formalize the fluid prediction problem as learning future fluid given past observation, as shown in Figure 2(d). Given a bounded open subset of d -dimensional

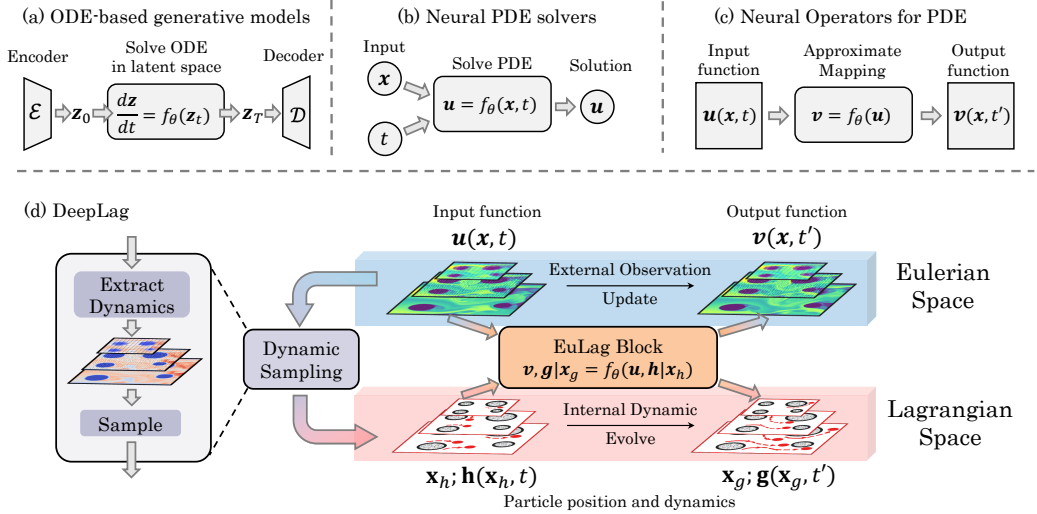


Figure 2: Three types of neural fluid prediction models (a-c) and overview of DeepLag (d). The EuLag Block accumulates the previous dynamics at each time and scale to guide the Eulerian field update and then evolves the particle movement and dynamic conditioned on the updated field.

Euclidean space $\mathcal{D} \subset \mathbb{R}^d$, a fluid with o observed quantities can be seen as functions of coordinates in Banach space $\mathcal{U} = \mathcal{U}(\mathcal{D}; \mathbb{R}^o)$. $\mathbf{u}_t(\mathbf{x}) \in \mathbb{R}^o$ and $\mathbf{u}_{t+1}(\mathbf{x}) \in \mathbb{R}^o$ represent the fluid function at two consecutive time steps for the coordinate $\mathbf{x} \in \mathcal{D}$. Provided P step observations $U_P = \{\mathbf{u}_1, \dots, \mathbf{u}_P\}$, the fluid prediction process can be written as the following autoregressive paradigm:

$$\tilde{U}_t = \{\tilde{\mathbf{u}}_{t-P+1}, \dots, \tilde{\mathbf{u}}_t\} \xrightarrow{\mathcal{F}_\theta} \tilde{\mathbf{u}}_{t+1}, \quad (3)$$

where $t \geq P$ and \mathcal{F}_θ represents the learned mapping. $\tilde{U}_t = U_t$ if $t = P$ and $\tilde{\mathbf{u}}_{t'} = \mathbf{u}_{t'}$ if $t' \leq P$.

Inspired by Eq. (2), we present DeepLag as an Eulerian-Lagrangian Recurrent Network, which utilizes EuLag Block to learn Eulerian features and important Lagrangian dynamics interactively at various scales to address the complex spatiotemporal correlations in fluid prediction. Specifically, we capture the temporal evolving features at fixed points from the Eulerian perspective and the spatial dynamic information of essential particles from the Lagrangian perspective through their movement. By integrating Lagrangian pivotal dynamic information into Eulerian features, we fully model the spatiotemporal evolution of the fluid field over time and motion. Moreover, DeepLag can obtain critical trajectories within fluid dynamics with high computational efficiency by incorporating high-dimensional Eulerian space into lower-dimensional Lagrangian space.

3.1 Overall Framework

It is widely acknowledged that fluids exhibit different motion characteristics across varying scales [3, 52]. In order to capture the intrinsic dynamics information at different scales, we track the trajectories of the key particles on these scales separately and propose an Eulerian-Lagrangian Recurrent Network to realize the interaction between Eulerian and Lagrangian information.

Initializing Lagrangian particles To better capture the complex dynamics within the fluid field, we sample crucial points from the given observations in the Eulerian perspective to determine the initial position for Lagrangian tracking in the dynamic sampling module. Explicitly, for the first predicting step, i.e. $t = P$, given observations $\mathbf{u}_t^l = \{\mathbf{u}_t^l(\mathbf{x}_k) | \mathbf{x}_k \in \mathcal{D}, 1 \leq k \leq N\} \in \mathbb{R}^{N \times C}$ on all N points with C channels at the l -th scale, we extract their spatial dynamics by a convolutional structure. We then calculate the probability matrix $\mathbf{S}^l \in \mathbb{R}^N$ using softmax along spatial dimension:

$$\mathbf{S}^l = \text{Softmax}(\text{ConvNet}(\mathbf{u}_t^l)), \quad (4)$$

where $\text{ConvNet}(\cdot)$ consists of a convolutional, activation, and fully-connected layer. We then sampled M_l tracking particles using the probability matrix at the l -th scale,

$$\mathbf{x}_h^l = \mathbf{p}_t^l = \text{Sample}(\{\mathbf{x}_k\}_{k=1}^N, \mathbf{S}), \quad (5)$$

where $\mathbf{p}_t^l = \{\mathbf{p}_{t,i}^l \in \mathcal{D}\}_{i=1}^{M_l} \in \mathbb{R}^{M_l \times d}$ represents the set of sampled M_l particles.

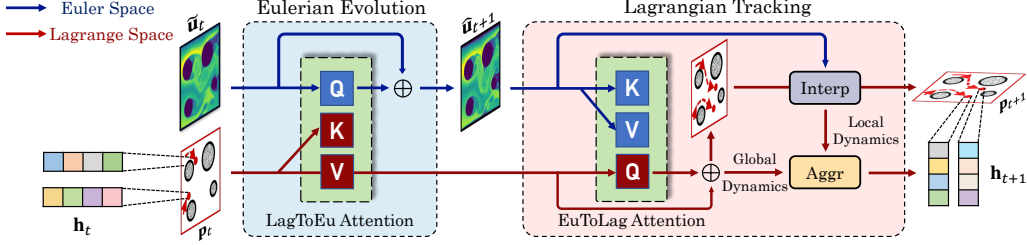


Figure 3: Overview of the EuLag Block, which accumulates previous dynamics information to guide Eulerian evolution for predicting particle movement. Scale index l is omitted.

Eulerian Fluid Prediction with Lagrangian Dynamics For the t -th step, we adopt a learnable embedding layer with multiscale architecture to encode past observations or predictions $\{\tilde{\mathbf{u}}_{t-P+1}, \dots, \tilde{\mathbf{u}}_t\}$ to obtain the Eulerian representations $\tilde{\mathbf{u}}_t^l : \mathcal{D}_l \rightarrow \mathbb{R}^{C_l}$, where $l \in \{1, 2, \dots, L\}$, and $\mathcal{D}_l \subset \mathbb{R}^d$ denotes the corresponding downsampled observation domain.

At each scale, we integrate EuLag Block to fuse the Lagrangian dynamics, thus directing the evolution of Eulerian features. This interaction also enables Eulerian features to guide the progression of Lagrangian dynamics. For the l -th scale, we track M_l key particles over time, with $\mathbf{x}_h^l = \mathbf{p}_t^l = \{\mathbf{p}_{t,i}^l \in \mathcal{D}_l\}_{i=1}^{M_l}$ representing their positions and $\mathbf{h}_t^l(\mathbf{x}_h^l) = \mathbf{h}_t^l = \{\mathbf{h}_{t,i}^l\}_{i=1}^{M_l} \in \mathbb{R}^{C_l \times M_l}$ denoting their learned particle dynamics. As shown in Figure 2(d), the positions and dynamics of particles at the l -th scale are learned autoregressively using the EuLag Block, which can be written as:

$$\hat{\mathbf{u}}_{t+1}, \{\mathbf{p}_{t+1}\}, \{\mathbf{h}_{t+1}\} = \text{EuLag}(\tilde{\mathbf{u}}_t, \{\mathbf{p}_t\}, \{\mathbf{h}_t\}), \quad (6)$$

where the scale index l is omitted. The EuLag Block optimally leverages the complementary strengths of Eulerian and Lagrangian representations, facilitating enhanced training and mutual refinement between these two perspectives. More details about the implementation of the EuLag Block are expanded in the following subsection.

After getting the output Eulerian features $\hat{\mathbf{u}}_{t+1}^l$ with Lagrangian particle position $\mathbf{x}_g^l = \mathbf{p}_{t+1}^l$ and dynamics $\mathbf{g}_t^l(\mathbf{x}_g^l) = \mathbf{h}_{t+1}^l$, we further aggregated $\hat{\mathbf{u}}_{t+1}^l$ with $\tilde{\mathbf{u}}_{t+1}^{l+1}$ at coarser scale by upsampling $\text{Up}(\cdot)$ to be $\tilde{\mathbf{u}}_{t+1}^l$. Eventually, the prediction $\tilde{\mathbf{u}}_{t+1}$ at step $t+1$ is decoded from $\tilde{\mathbf{u}}_{t+1}^1$ with a projection layer. We unfold the implementation of the overall architecture in Appendix A.2.

3.2 EuLag Block

As formalized in Eq. (6), we adopt a recurrent framework to interactively exploit the information from Eulerian and Lagrangian perspectives, which consist of two main components: Lagrangian-guided feature evolving and Eulerian-conditioned particle tracking. For clarity, we omit the scale index in this section. The following quantities are all in the l -th scale.

Lagrangian-guided feature evolving Classical theories [9] and numerical algorithms [31] showed that fluid predictions can be solved by identifying the origin of the fluid parcel and interpolating the dependent variable from nearby grid points. However, without specifying certain PDEs, we cannot explicitly determine the former position of the particle on each Eulerian observed point. Thus, we first adaptively synthesize the Lagrangian dynamics of the tracked particles to guide the evolution of Eulerian features using a cross-attention mechanism. Expressly, we adopt a Lagrangian-to-Eulerian attention, where the Eulerian field $\tilde{\mathbf{u}}_t$ serves as queries, and Lagrangian dynamics with particle position $\mathbf{h}_t' = \text{Concat}(\mathbf{h}_t, \mathbf{p}_t) \in \mathbb{R}^{M \times (C+d)}$ is used as keys and values:

$$\text{LagToEu_Attn}(\tilde{\mathbf{u}}_t^l, \mathbf{h}_t^l, \mathbf{h}_t') = \text{Softmax} \left(\frac{\mathbf{W}_Q \tilde{\mathbf{u}}_t^l (\mathbf{W}_K \mathbf{h}_t')^T}{\sqrt{C+d}} \right) \mathbf{W}_V \mathbf{h}_t', \quad (7)$$

where \mathbf{W}_Q , \mathbf{W}_K and \mathbf{W}_V stand for linear projection layers. We summarize the above Lagrangian dynamics guided Eulerian Evolution process as $\hat{\mathbf{u}}_{t+1}^l = \tilde{\mathbf{u}}_t^l + \text{LagToEu}(\tilde{\mathbf{u}}_t^l, \mathbf{h}_t^l, \mathbf{h}_t')$.

Eulerian-conditioned particle tracking Traditional Lagrangian methods rely on interactions among vast quantities of particles to estimate the future fluid fields. However, the high computational

cost hinders the application in rapid, deep models. In other data-driven approaches, the sparse sampling of tracking particles is computational-friendly but cannot directly derive Lagrangian dynamics for every particle. Considering the equivalence of the Eulerian and Lagrangian representations indicated in Eq. (1), we propose to learn particle movements based on the Eulerian conditions. Concretely, we utilize another Eulerian-to-Lagrangian cross-attention, where the evolved Eulerian features of the whole fluid field are used to navigate the Lagrangian dynamics of sparse particles:

$$\begin{aligned} \mathbf{p}_{t+1} &= \text{TrmBlock}_{Q, K, V_p}(\mathbf{h}'_t, \hat{\mathbf{u}}_{t+1}) \\ \mathbf{h}_{\text{global}, t+1} &= \text{TrmBlock}_{Q, K, V_h}(\mathbf{h}'_t, \hat{\mathbf{u}}_{t+1}), \end{aligned} \quad (8)$$

where $\text{TrmBlock}_{Q, K, V}(\cdot, \cdot)$ represents standard transformer block with $\mathbf{W}'_Q, \mathbf{W}'_K, \mathbf{W}'_V$ as linear projection matrix. The forecasted global Lagrangian dynamic and movement of tracking particles are produced by two transformers with the same query and key projection but different value projections. To better model the dynamic evolution of the particles, we gather local Lagrangian dynamic by employing bilinear interpolation to output Eulerian features $\hat{\mathbf{u}}_{t+1}$ on particles \mathbf{p}_{t+1} , then use a linear function to interact with global dynamics information $\mathbf{h}_{\text{global}, t+1}$, naming $\mathbf{h}_{t+1} = \text{Aggregate}(\hat{\mathbf{u}}_{t+1}, \mathbf{p}_{t+1}, \mathbf{h}_{\text{global}, t+1})$. Additionally, as the input flow field may have an open boundary, the particles could move out of the observation domain. We check the position of the particles and resample them in case they exit. Similar to the previous Eulerian Evolution process, the above Lagrangian Tracking process is summarized as EuToLag(\cdot).

Overall, the EuLag Block can fully utilize the complementary advantages of Eulerian and Lagrangian perspectives in describing fluid dynamics, thereby being better suited to fluid prediction. For more implementation details of the EuLag Block, please refer to Appendix A.3.

4 Experiments

We evaluated DeepLag on three challenging benchmarks, including simulated and real-world scenarios, covering both 2D and 3D, as well as single and multi-physics fluids. Following the previous convention [21], we train DeepLag and the baselines for each task to predict ten future timesteps in an autoregressive fashion given ten past observations. Detailed benchmark information is listed in Table 1. We provide an elaborate analysis of the efficiency, parameter count, and performance difference in section 4.4 and Appendix E. Additionally, more detailed visualizations, besides in later this section, are provided in Appendix H. Furthermore, the trained models are engaged to perform 30 frames extrapolation to examine their long-term stability.

Baselines To demonstrate the effectiveness of our model, we compare DeepLag with seven baselines on all benchmarks, including the classical multiscale model U-Net [32] and advanced neural operators for Navier-Stokes equations: FNO [21], Galerkin Transformer [3], Vortex for 2D image [7], GNOT [14], LSM [52] and FactFormer [20]. U-Net has been widely used in fluid modeling, which can model the multiscale property precisely. LSM [52] and FactFormer [20] are previous state-of-the-art neural operators.

Metrics For all three tasks, we follow the convention in neural fluid prediction [21, 52] and report relative L2 as the main metric. Implementations of the metrics are included in Appendix A.4.

Implementations Aligned with convention and the baselines, DeepLag is trained with relative L2 as the loss function on all benchmarks. We use the Adam [18] optimizer with an initial learning rate of 5×10^{-4} and StepLR learning rate scheduler. The batch size is set to 5, and the training process is stopped after 100 epochs. All experiments are implemented in PyTorch [24] and conducted on a single NVIDIA A100 GPU. Training curves are shown in Appendix D.

4.1 Bounded Navier-Stokes

Setups In real-world applications, handling complex boundary conditions in predicting fluid dynamics is indispensable. Thus, we experiment with the newly generated Bounded Navier-Stokes,

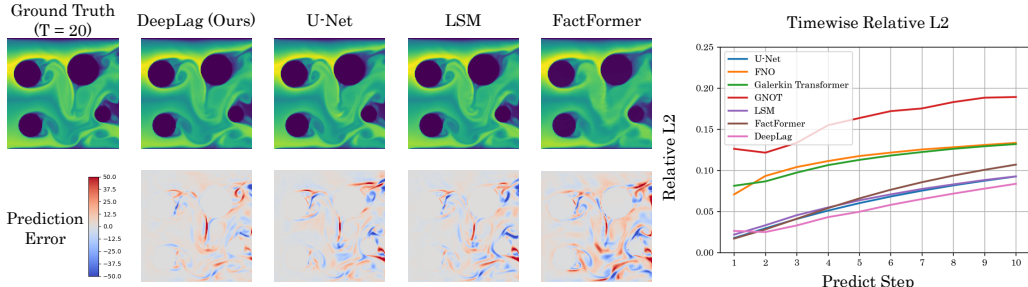


Figure 4: Showcases and timewise relative L2 on Bounded Navier-Stokes dataset. Both predictions and absolute error maps are plotted.

which simulates a scenario where some colored dye flows from left to right through a 2D pipe with several fixed pillars as obstacles inside. Details about this benchmark can be found in Appendix C.1.

Quantitive results As shown in Table 2, DeepLag achieves the best performance on Bounded Navier-Stokes, demonstrating its advanced ability to handle complex boundary conditions. In comparison to the previous best model, DeepLag achieves a significant 13.8% (Relative L2: 0.0618 v.s. 0.0544) and 2.7% (Relative L2: 0.1020 v.s. 0.0993) relative promotion on short and long rollout. The timewise error curves of all the models are also included in Figure 4. We can find that DeepLag presents slower error growth and excels in long-term forecasting. This result may stem from the Lagrangian-guided fluid prediction, which can accurately capture the dynamics information over time, further verifying the effectiveness of our design.

Showcases To intuitively present the forecasting skills of different models, we also provide showcase comparisons in Figure 4. We can find that DeepLag can precisely illustrate the vortex in the center of the figure and the Kármán vortex phenomenon formed behind the upper left pillar. As for U-Net and LSM, although they successfully predicted the position of the center vortex, the error map shows that they failed to predict the density field accurately. In addition, FactFormer deteriorates on this benchmark. This may be because it is based on spatial factorization, which is unsuitable for irregularly placed boundary conditions. These results further highlight the benefits of Eulerian-Lagrangian co-design, which can simultaneously help with dynamic and density prediction.

4.2 Ocean Current

Setups Predicting large-scale ocean currents, especially in regions near tectonic plate boundaries prone to disasters such as tsunamis due to intense terrestrial activities, plays a crucial role in various domains. Hence, we also explore this valuable scenario in our experiments. More details about this benchmark can be found in Appendix C.2.

Quantitive results We report relative L2 for the Ocean Current dataset in Table 3, where DeepLag still achieves the best with 8.3% relative promotion w.r.t. the second-best model.

Table 2: Performance comparison on Bounded Navier-Stokes. Relative L2 of 10 frames and 30 frames prediction are recorded. Promotion represents the relative promotion of DeepLag w.r.t the second-best (underlined). “NaN” refers to the instability during rollout.

Model	Relative L2 (↓)	
	10 Frames	30 Frames
U-Net [32]	<u>0.0618</u>	0.1038
FNO [21]	0.1041	0.1282
Galerkin Transformer [3]	0.1084	0.1369
Vortex [7]	0.1999	NaN
GNOT [14]	0.1388	0.1793
LSM [52]	0.0643	<u>0.1020</u>
FactFormer [20]	0.0733	0.1195
DeepLag (Ours)	0.0543	0.0993
Promotion	13.8%	2.7%

Table 3: Performance comparison on Ocean Current. We report the relative L2 of the short-term and long-term rollouts with their relative promotions.

Model	Relative L2 (↓)	
	10 Days	30 Days
U-Net [32]	0.0185	0.0297
FNO [21]	0.0246	0.0420
Galerkin Transformer [3]	0.0323	0.0515
Vortex [7]	0.9548	NaN
GNOT [14]	0.0206	0.0336
LSM [52]	<u>0.0182</u>	<u>0.0290</u>
FactFormer [20]	0.0183	0.0296
DeepLag (Ours)	0.0168	0.0257
Promotion	8.3%	12.8%

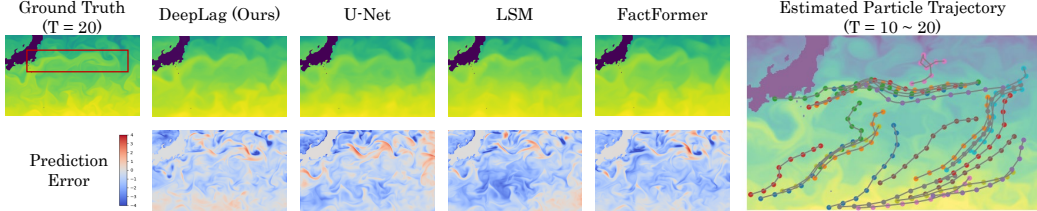


Figure 5: Showcase comparison and visualization of Lagrangian trajectories learned by DeepLag on Ocean Current. Notably, potential temperatures predicted by different models are plotted. Error maps of predictions are normalized to $(-4, 4)$ for a better view.

Even in 30 days of forecasting, the number is 12.8%. These results show that DeepLag performs well in real-world, large-scale fluids, which usually involve more inherent stochasticity than simulated data. Moreover, we provide the ACC metric and timewise curve in Appendix F.

Showcases We presented different model predictions in Figure 5. In comparison to other models, DeepLag exhibits the most minor prediction error. It accurately predicts the location of the high-temperature region to the south area and provides a clear depiction of the Kuroshio pattern [37] bounded by the red box.

Learned trajectory visualization To reveal the effect of learning Lagrangian trajectories, we visualize tracked particles in Figure 5. We observe that all the particles move from west to east, consistent with the Pacific circulation. Additionally, the tracked particles show distinct moving patterns, confirming their ability to represent complex dynamics. The movement of upper particles matches the sinuous trajectory of the Kuroshio current, demonstrating the capability of DeepLag to provide interpretable evidence for prediction results. Visualizing the tracking points in Lagrangian space instills confidence in the reliability and interpretability of the predictions made by our system.

4.3 3D Smoke

Setups 3D fluid prediction has been a long-standing challenge due to the tanglesome dynamics involved. Therefore, we created this benchmark to describe a scenario in which smoke flows under the influence of buoyancy in a three-dimensional bounding box. For more details, please refer to Appendix C.3.

Quantitive results Table 4 shows that DeepLag still performs best in 3D fluid. Note that in this benchmark, the canonical deep model U-Net degenerates seriously, indicating that a pure Eulerian multiscale framework is insufficient to model complex dynamics. We also noticed that the Transformer-based neural operators, such as GNOT and Galerkin Transformer, failed in this task. This may be because both of them are based on the linear attention mechanism [19, 54], which may deprecate under massive tokens. These comparisons further highlight the capability of DeepLag to handle high-dimensional fluid.

Showcases In Figure 6, we compared prediction results on the 3D Smoke dataset. DeepLag performs well in capturing the convection and diffusion of smoke within the bounding box. In comparison, the predictions of U-Net tend to predict the averaged value across various surfaces, resulting in blurred details, which also indicates its deficiency in dynamics modeling. As for LSM and FactFormer, we can find that they present more errors in the smoke boundaries that usually involve complex waves. In contrast, our model excels in overall and cross-section error and performs excellently in predicting subtle flows.

4.4 Model Analysis

Ablations To verify the effectiveness of detailed designs in DeepLag, we conduct exhaustive ablations in Table 5. In our original design, we track 512 particles (around 3% of Eulerian grids).

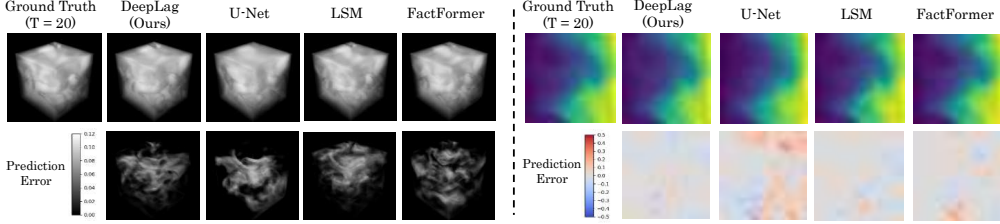


Figure 6: Showcases comparison of the whole space (left part) and a cross-section (right part) on 3D Smoke dataset. For better visualization, we present the absolute value of the prediction error and normalize the whole space error into $(0, 0.12)$. As for the cross-section visualization, we choose the xOy plane in the middle 3D fluid and normalize error maps to $(-0.5, 0.5)$.

The experiments indicate that further increasing the number of particles yields marginal performance improvements. Therefore, we opt for $M_1 = 512$ to strike a balance between efficiency and performance. In addition, we can conclude that all components proposed in this paper are indispensable. Especially, the lack of interaction between the Eulerian and Lagrangian space will cause a severe drop in accuracy, highlighting the dual cross-attention that exploits Lagrangian dynamics has a positive influence on the evolution of Eulerian features. Besides, rather than uniformly sampling particles, sampling from a learnable probability matrix also provides an upgrade (refer to Appendix G for visual results). The above results provide solid support to our motivation in tracking essential particles and utilizing Eulerian-Lagrangian recurrence, further confirming the merits of our model.

Efficiency analysis We also include the efficiency comparison in Figure 7. DeepLag hits a favorable balance between efficiency and performance by simultaneously considering performance, model parameters, and running time, demonstrating superior performance with significantly less memory than GNOT and LSM, thereby minimizing storage complexity. Standard U-Net has a large number of parameters, and Transformers have quadratic memory, so in large-scale or complex fluid prediction scenarios, using linear complexity attention mechanisms like ours is necessary. This explains why, although U-Net and LSM are good at Bounded Navier-Stokes, they will worsen when it comes to complex fluid dynamics, such as the Ocean Current and the 3D Smoke benchmark.

5 Conclusions and Limitations

To tackle intricate fluid dynamics, this paper presents DeepLag by introducing the Lagrangian dynamics into Eulerian fluid, which can provide clear and neat dynamics information for prediction. A *EuLag Block* is presented in the *Eulerian-Lagrangian Recurrent Network* to utilize the complementary advantages of Eulerian and Lagrangian perspectives, which brings better particle tracking and Eulerian fluid prediction. DeepLag excels in complex fluid prediction with an average improvement of nearly 10% across three carefully selected complex benchmarks, even in 3D fluid, and can also provide interpretable evidence by plotting learned Lagrangian trajectories. However, the number of tracking particles in DeepLag is appointed as a fixed hyperparameter that needs to be adjusted for specific scenarios, leaving space for future exploration.

Table 5: Ablations on Bounded Navier-Stokes, including reducing tracking particles of the first layer (M_1), removing Lagrangian-guided feature evolving $\text{LagToEu}(\cdot)$, Eulerian-conditioned particle tracking $\text{EuToLag}(\cdot)$ and learnable particle sampling strategy.

Design	Relative L2 (\downarrow)	Decrease
DeepLag ($M_1 = 512$)	0.0543	-
$M_1 = 128$	0.0559	2.9%
$M_1 = 256$	0.0553	1.8%
$M_1 = 768$	0.0547	0.7%
w/o $\text{LagToEu}(\cdot)$	0.0556	2.4%
w/o $\text{EuToLag}(\cdot)$	0.0547	0.7%
w/o Learnable Sampling	0.0552	1.6%

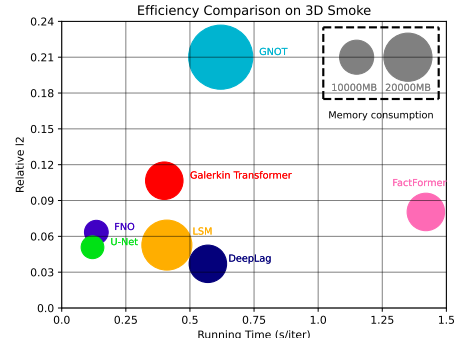


Figure 7: Efficiency comparison among all the models. Running time and Relative L2 are evaluated on the 3D Smoke benchmark.

References

- [1] G. K. Batchelor. *An Introduction to Fluid Dynamics*. Cambridge Mathematical Library. Cambridge University Press, 2000.
- [2] Johannes Brandstetter, Daniel E. Worrall, and Max Welling. Message passing neural PDE solvers. In *International Conference on Learning Representations*, 2022.
- [3] Shuhao Cao. Choose a transformer: Fourier or galerkin. In *Conference on Neural Information Processing Systems*, 2021.
- [4] Ricky T. Q. Chen, Yulia Rubanova, Jesse Bettencourt, and David K Duvenaud. Neural ordinary differential equations. In S. Bengio, H. Wallach, H. Larochelle, K. Grauman, N. Cesa-Bianchi, and R. Garnett, editors, *Advances in Neural Information Processing Systems*, volume 31. Curran Associates, Inc., 2018.
- [5] CMEMS and MDS. Global ocean physics reanalysis. DOI: 10.48670/moi-00021 (Accessed on 23 September 2023), 2023.
- [6] R. Courant, K. Friedrichs, and H. Lewy. On the partial difference equations of mathematical physics. *IBM Journal of Research and Development*, 11(2):215–234, 1967.
- [7] Yitong Deng, Hong-Xing Yu, Jiajun Wu, and Bo Zhu. Learning vortex dynamics for fluid inference and prediction. In *ICLR*, 2023.
- [8] Mahesh Dissanayake and Nhan Phan-Thien. Neural-network-based approximations for solving partial differential equations. *Communications in Numerical Methods in Engineering*, 1994.
- [9] L.C. Evans. *Partial Differential Equations*. Graduate studies in mathematics. American Mathematical Society, 2010.
- [10] Joel Ferziger, Milovan Perić, and Robert Street. *Computational Methods for Fluid Dynamics*. Springer Nature Switzerland, 2020.
- [11] Han Gao, Luning Sun, and Jian-Xun Wang. Phygeonet: Physics-informed geometry-adaptive convolutional neural networks for solving parameterized steady-state pdes on irregular domain. *Journal of Computational Physics*, 428:110079, March 2021.
- [12] Robert A. Gingold and Joseph John Monaghan. Smoothed particle hydrodynamics: Theory and application to non-spherical stars. *Monthly Notices of the Royal Astronomical Society*, 181:375–389, 1977.
- [13] K.C. Gupta. *Classical Mechanics of Particles and Rigid Bodies*. Wiley, 1988.
- [14] Zhongkai Hao, Chengyang Ying, Zhengyi Wang, Hang Su, Yinpeng Dong, Songming Liu, Ze Cheng, Jun Zhu, and Jian Song. Gnot: A general neural operator transformer for operator learning. In *International Conference on Machine Learning*, 2023.
- [15] Kaiming He, Xiangyu Zhang, Shaoqing Ren, and Jian Sun. Deep residual learning for image recognition, 2015.
- [16] Dan Hendrycks and Kevin Gimpel. Gaussian error linear units (gelus). *arXiv: Learning*, 2016.
- [17] Zichao Jiang, Junyang Jiang, Qinghe Yao, and Gengchao Yang. A neural network-based pde solving algorithm with high precision. *Nature News*, Mar 2023.
- [18] Diederik P. Kingma and Jimmy Ba. Adam: A method for stochastic optimization. In *International Conference on Learning Representations*, 2015.
- [19] Nikita Kitaev, Lukasz Kaiser, and Anselm Levskaya. Reformer: The efficient transformer. In *International Conference on Learning Representations*, 2020.
- [20] Zijie Li, Dule Shu, and Amir Barati Farimani. Scalable transformer for pde surrogate modeling. In *Conference on Neural Information Processing Systems*, 2023.
- [21] Zongyi Li, Nikola Borislavov Kovachki, Kamyar Azizzadenesheli, Burigede liu, Kaushik Bhattacharya, Andrew Stuart, and Anima Anandkumar. Fourier neural operator for parametric partial differential equations. In *International Conference on Learning Representations*, 2021.
- [22] Lu Lu, Pengzhan Jin, Guofei Pang, Zhongqiang Zhang, and George Em Karniadakis. Learning nonlinear operators via deeponet based on the universal approximation theorem of operators. *Nature Machine Intelligence*, 2021.

[23] Faith A Morrison. *An introduction to fluid mechanics*. Cambridge University Press, 2013.

[24] Adam Paszke, Sam Gross, Francisco Massa, Adam Lerer, James Bradbury, Gregory Chanan, Trevor Killeen, Zeming Lin, Natalia Gimelshein, Luca Antiga, et al. Pytorch: An imperative style, high-performance deep learning library. *Advances in Neural Information Processing Systems*, 2019.

[25] Tobias Pfaff, Meire Fortunato, Alvaro Sanchez-Gonzalez, and Peter Battaglia. Learning mesh-based simulation with graph networks. In *International Conference on Learning Representations*, 2021.

[26] Gavin D. Portwood, Peetak P. Mitra, Mateus Dias Ribeiro, Tan Minh Nguyen, Balasubramanya T. Nadiga, Juan A. Saenz, Michael Chertkov, Animesh Garg, Anima Anandkumar, Andreas Dengel, Richard Baraniuk, and David P. Schmidt. Turbulence forecasting via neural ode, 2019.

[27] Md Ashiqur Rahman, Zachary E Ross, and Kamyar Azizzadenesheli. U-no: U-shaped neural operators. *TMLR*, 2023.

[28] Maziar Raissi, Paris Perdikaris, and George Em Karniadakis. Physics informed deep learning (part i): Data-driven solutions of nonlinear partial differential equations. *arXiv preprint*, 2017.

[29] Maziar Raissi, Paris Perdikaris, and George Em Karniadakis. Physics-informed neural networks: A deep learning framework for solving forward and inverse problems involving nonlinear partial differential equations. *Journal of Computational Physics*, 2019.

[30] Bogdan Raonic, Roberto Molinaro, Tim De Ryck, Tobias Rohner, Francesca Bartolucci, Rima Alaifari, Siddhartha Mishra, and Emmanuel de Bezenac. Convolutional neural operators for robust and accurate learning of PDEs. In *Thirty-seventh Conference on Neural Information Processing Systems*, 2023.

[31] André Robert. A stable numerical integration scheme for the primitive meteorological equations. *Atmosphere-Ocean*, 19(1):35–46, 1981.

[32] Olaf Ronneberger, Philipp Fischer, and Thomas Brox. U-net: Convolutional networks for biomedical image segmentation. In *The Medical Image Computing and Computer Assisted Intervention Society*, 2015.

[33] Alvaro Sanchez-Gonzalez, Jonathan Godwin, Tobias Pfaff, Rex Ying, Jure Leskovec, and Peter W. Battaglia. Learning to simulate complex physics with graph networks. In *International Conference on Machine Learning*, 2020.

[34] Connor Schenck and Dieter Fox. Spnets: Differentiable fluid dynamics for deep neural networks, 2018.

[35] Fabio Sim, Eka Budiarto, and Rusman Rusyadi. Comparison and analysis of neural solver methods for differential equations in physical systems. *ELKHA: Jurnal Teknik Elektro*, 2021.

[36] takah29, houkensjtu, and zemora. 2d incompressible fluid solver implemented in taichi, 2023.

[37] TY Tang, JH Tai, and YJ Yang. The flow pattern north of taiwan and the migration of the kuroshio. *Continental Shelf Research*, 2000.

[38] Roger Temam. *Navier-Stokes equations: theory and numerical analysis*. American Mathematical Soc., 2001.

[39] Eleuterio Toro. *Riemann Solvers and Numerical Methods for Fluid Dynamics: A Practical Introduction*. 2009.

[40] Gerard V. Trunk. A problem of dimensionality: A simple example. *IEEE Transactions on Pattern Analysis and Machine Intelligence*, 1979.

[41] Nobuyuki Umetani and Bernd Bickel. Learning three-dimensional flow for interactive aerodynamic design. *ACM Transactions on Graphics (TOG)*, 2018.

[42] Benjamin Ummenhofer, Lukas Prantl, Nils Thuerey, and Vladlen Koltun. Lagrangian fluid simulation with continuous convolutions. In *International Conference on Learning Representations*, 2020.

[43] Ashish Vaswani, Noam Shazeer, Niki Parmar, Jakob Uszkoreit, Llion Jones, Aidan N Gomez, Łukasz Kaiser, and Illia Polosukhin. Attention is all you need. In *NeurIPS*, 2017.

[44] Nils Wandel, Michael Weinmann, Michael Neidlin, and Reinhard Klein. Spline-pinn: Approaching pdes without data using fast, physics-informed hermite-spline cnns, 2022.

[45] Hanchen Wang, Tianfan Fu, Yuanqi Du, Wenhao Gao, Kexin Huang, Ziming Liu, Payal Chandak, Shengchao Liu, Peter Van Katwyk, Andreea Deac, et al. Scientific discovery in the age of artificial intelligence. *Nature*, 2023.

[46] Sifan Wang, Yujun Teng, and Paris Perdikaris. Understanding and mitigating gradient pathologies in physics-informed neural networks. *SIAM Journal on Scientific Computing*, 2020.

[47] Sifan Wang, Xinling Yu, and Paris Perdikaris. When and why pinns fail to train: A neural tangent kernel perspective. *Journal of Computational Physics*, 2020.

[48] E Weinan and Ting Yu. The deep ritz method: A deep learning-based numerical algorithm for solving variational problems. *Communications in Mathematics and Statistics*, 2017.

[49] F.M. White. *Fluid Mechanics*. McGraw-Hill series in mechanical engineering. 2011.

[50] R Wille. Karman vortex streets. *Advances in Applied Mechanics*, 1960.

[51] Nick Winovich, Karthik Ramani, and Guang Lin. Convpde-uq: Convolutional neural networks with quantified uncertainty for heterogeneous elliptic partial differential equations on varied domains. *J. Comput. Phys.*, 394(C):263–279, oct 2019.

[52] Haixu Wu, Tengge Hu, Huakun Luo, Jianmin Wang, and Mingsheng Long. Solving high-dimensional pdes with latent spectral models. In *International Conference on Machine Learning*, 2023.

[53] Ruibin Xiong, Yunchang Yang, Di He, Kai Zheng, Shuxin Zheng, Chen Xing, Huishuai Zhang, Yanyan Lan, Liwei Wang, and Tie-Yan Liu. On layer normalization in the transformer architecture, 2020.

[54] Yunyang Xiong, Zhanpeng Zeng, Rudrasis Chakraborty, Mingxing Tan, Glenn M. Fung, Yin Li, and Vikas Singh. Nyströmformer: A nyström-based algorithm for approximating self-attention. *Proceedings of the AAAI Conference on Artificial Intelligence*, 2021.

[55] Cagatay Yıldız, Markus Heinonen, and Harri Lahdesmaki. Ode2vae: Deep generative second order odes with bayesian neural networks. In H. Wallach, H. Larochelle, A. Beygelzimer, F. d'Alché-Buc, E. Fox, and R. Garnett, editors, *Advances in Neural Information Processing Systems*, volume 32. Curran Associates, Inc., 2019.

A Implementation Details

This section provides the implementation details of DeepLag, including the configurations of model hyperparameters and the concrete design of modules.

A.1 Hyperparameters

Detailed model configurations of DeepLag are listed in Table 6. Zero-padding is only used in the Ocean Current dataset to ensure the exact division in downsampling.

Table 6: Model configurations for DeepLag.

Model Designs	Hyperparameters	Values
Eulerian-Lagrangian Recurrent Network	Number of observation steps P	10
	Number of scales L	4
	Sample Points at each scale $\{M_1, \dots, M_L\}$	$\{512, 128, 32, 8\}$
	Downsample Ratio $r = \frac{ \mathcal{D}_{l+1} }{ \mathcal{D}_l }$	0.5
	Channels of each scale $\{C_1, \dots, C_L\}$	$\{64, 128, 256, 256\}$
EuLag Block	Paddings for Ocean Current dataset	(12, 20)
	Heads in Cross-Attention	8
	Channels per head in Cross-Attention	64

A.2 Sampling and multiscale architecture in overall framework

A.2.1 Sampling to initialize Lagrangian particles

At the first predicting step, the position of Lagrangian particles to track is initialized by the *dynamic sampling* module consisting of dynamics extracting and sampling.

The Extract(\cdot) to extract dynamics Given the Eulerian input function $\{\tilde{u}_t^l(\mathbf{x})\}_{\mathbf{x} \in \mathcal{D}_l}$ at the l -th scale, the Extract(\cdot) operation in Eq. (4) is to extract the local dynamics around each Eulerian observation point with Conv(), BatchNorm() and ReLU() layers, which can be formalized as follows:

$$\text{Extract}(\tilde{u}_t) = \text{Conv} \left(\text{ReLU} \left(\text{BatchNorm} \left(\text{Conv}(\{\tilde{u}_t^l(\mathbf{x})\}_{\mathbf{x} \in \mathcal{D}_l}) \right) \right) \right), \quad l \text{ from 1 to } L. \quad (9)$$

Here, the output channel of the outermost Conv is 1.

The Sample(\cdot) to select key particles Given the probability distribution matrix $\mathbf{S}_t^l(\mathbf{x})_{\mathbf{x} \in \mathcal{D}_l}$ and the number of particles to sample M_l at the l -th scale, we choose the particles for further tracking by Multinomial(\cdot) without replacement:

$$\text{Sample}(\mathbf{S}_t^l) = \text{Multinomial}(\mathbf{S}_t^l, M_l), \quad l \text{ from 1 to } L. \quad (10)$$

A.2.2 Multiscale architecture

Multiscale modeling is utilized in DeepLag as represented in Figure 2(d), where we need to maintain multiscale deep Eulerian features as follows:

Encoder Given Eulerian fluid function $\{\tilde{u}_t(\mathbf{x})\}_{\mathbf{x} \in \mathcal{D}}$ at the t -th time step, $\{\tilde{u}_{(t-P+1):(t-1)}(\mathbf{x})\}_{\mathbf{x} \in \mathcal{D}}$ at previous time steps and the 0-1 boundary-geometry mask $\{\mathbf{m}(\mathbf{x})\}_{\mathbf{x} \in \mathcal{D}}$ where 1 indicates the border and the unreachable area (like pillars in Bounded Navier-Stokes), the Encode() operation is to project original fluid properties in physical domain to deep representations with linear layer and position embedding, which can be formalized as follows:

$$\tilde{u}_t^1 = \text{Linear} \left(\text{Concat} \left(\{\tilde{u}_{(t-P+1):(t-1)}(\mathbf{x}), \mathbf{m}(\mathbf{x})\}_{\mathbf{x} \in \mathcal{D}} \right) \right) + \text{PosEmbedding}. \quad (11)$$

Decoder Given evolved Eulerian deep representations in the finest scale $\{\tilde{u}_{t+1}^1(\mathbf{x})\}_{\mathbf{x} \in \mathcal{D}}$ at the $(t+1)$ -th time step, the Decode() operation is to project deep representations back to predicted fluid properties with two linear layers and a GeLU activation [16], which can be formalized as follows:

$$\tilde{u}_{t+1} = \text{Linear} \left(\text{GeLU} \left(\text{Linear} \left(\{\tilde{u}_{t+1}^1(\mathbf{x})\}_{\mathbf{x} \in \mathcal{D}} \right) \right) \right). \quad (12)$$

Downsample Given Eulerian deep representations $\{\tilde{\mathbf{u}}_t^l(\mathbf{x})\}_{\mathbf{x} \in \mathcal{D}_l}$ at the l -th scale, the Down() operation is to concentrate local information of deep representations into a smaller feature map at the $(l+1)$ -th scale with MaxPooling() and Conv() layers, which can be formalized as follows:

$$\tilde{\mathbf{u}}_t^{l+1} = \text{Conv} \left(\text{MaxPooling} \left(\{\tilde{\mathbf{u}}_t^l(\mathbf{x})\}_{\mathbf{x} \in \mathcal{D}_l} \right) \right), \quad l \text{ from } 1 \text{ to } (L-1). \quad (13)$$

Upsample Given the evolved Eulerian deep representations $\{\tilde{\mathbf{u}}_{t+1}^l(\mathbf{x})\}_{\mathbf{x} \in \mathcal{D}_l}$ at the l -th scale and $\{\tilde{\mathbf{u}}_{t+1}^{l+1}(\mathbf{x})\}_{\mathbf{x} \in \mathcal{D}_{l+1}}$ at the $(l+1)$ -th scale, respectively, the Up() operation is to fuse information on corresponding position between two adjacent scales of deep representations into a feature map at the l -th scale with Interpolate() operation and Conv() layers, which can be formalized as follows:

$$\tilde{\mathbf{u}}_{t+1}^l = \text{Conv} \left(\text{Concat} \left(\left[\text{Interpolate} \left(\{\tilde{\mathbf{u}}_{t+1}^{l+1}(\mathbf{x})\}_{\mathbf{x} \in \mathcal{D}_{l+1}}, \{\tilde{\mathbf{u}}_{t+1}^l(\mathbf{x})\}_{\mathbf{x} \in \mathcal{D}_l} \right) \right] \right) \right), \quad l \text{ from } (L-1) \text{ to } 1 \quad (14)$$

A.3 EuLag Block

The LagToEu(\cdot) process As we stated in subsection 3.2, the Lagrangian-guided Eulerian feature evolving process, short as LagToEu(\cdot), aggregates information from Lagrangian description to guide the update of Eulerian field with a single Transformer layer at each scale:

$$\begin{aligned} \hat{\mathbf{u}}_{t+1}^l &= \tilde{\mathbf{u}}_t^l + \text{LagToEu}(\tilde{\mathbf{u}}_t^l, \mathbf{h}_t^l, \mathbf{h}_t^l) \\ &= \tilde{\mathbf{u}}_t^l + \text{FFN}(\text{LagToEu_Attn}(\tilde{\mathbf{u}}_t^l, \mathbf{h}_t^l, \mathbf{h}_t^l)) + \text{LagToEu_Attn}(\tilde{\mathbf{u}}_t^l, \mathbf{h}_t^l, \mathbf{h}_t^l), \quad l \text{ from } 1 \text{ to } L, \end{aligned} \quad (15)$$

where LagToEu_Attn($\tilde{\mathbf{u}}_t^l, \mathbf{h}_t^l, \mathbf{h}_t^l$) is described as Eq. (7). Moreover, we use the pre-normalization [53] technique for numerical stability.

The EuToLag(\cdot) process Similar to above, we acquire the new particle position \mathbf{p}_{t+1}^l and the global dynamics $\mathbf{h}_{\text{global},t+1}^l$ in the Eulerian-conditioned particle tracking by a Eulerian-Lagrangian cross-attention:

$$\begin{aligned} \mathbf{p}_{t+1}^l &= \text{TrmBlock}_{Q,K,V_p}(\mathbf{h}_t^l, \hat{\mathbf{u}}_{t+1}^l) \\ &= \mathbf{p}_t^l + \text{FFN} \left(\text{Softmax} \left(\frac{Q\mathbf{h}_t^l(K\hat{\mathbf{u}}_{t+1}^l)^T}{\sqrt{C}} \right) V_p \hat{\mathbf{u}}_{t+1}^l \right) + \text{Softmax} \left(\frac{Q\mathbf{h}_t^l(K\hat{\mathbf{u}}_{t+1}^l)^T}{\sqrt{C}} \right) V_p \hat{\mathbf{u}}_{t+1}^l, \end{aligned} \quad (16)$$

$$\begin{aligned} \mathbf{h}_{\text{global},t+1}^l &= \text{TrmBlock}_{Q,K,V_h}(\mathbf{h}_t^l, \hat{\mathbf{u}}_{t+1}^l) \\ &= \mathbf{h}_t^l + \text{FFN} \left(\text{Softmax} \left(\frac{Q\mathbf{h}_t^l(K\hat{\mathbf{u}}_{t+1}^l)^T}{\sqrt{C}} \right) V_h \hat{\mathbf{u}}_{t+1}^l \right) + \text{Softmax} \left(\frac{Q\mathbf{h}_t^l(K\hat{\mathbf{u}}_{t+1}^l)^T}{\sqrt{C}} \right) V_h \hat{\mathbf{u}}_{t+1}^l, \end{aligned} \quad (17)$$

where $l \in \{1, 2, \dots, L\}$. Then, we interpolate from $\hat{\mathbf{u}}_{t+1}^l$ by \mathbf{p}_{t+1}^l to be the local dynamics $\mathbf{h}_{\text{local},t+1}^l$ and Aggrerate it with the global dynamics $\mathbf{h}_{\text{global},t+1}^l$ using a Linear layer:

$$\mathbf{h}_{t+1} = \text{Aggregate}(\hat{\mathbf{u}}_{t+1}, \mathbf{p}_{t+1}, \mathbf{h}_{\text{global},t+1}) = \text{Linear} \left(\text{Concat} \left(\mathbf{h}_{\text{global},t+1}^l, \text{Interp}(\hat{\mathbf{u}}_{t+1}^l, \mathbf{p}_{t+1}^l) \right) \right). \quad (18)$$

A.4 Metrics

Relative L2 We use the relative L2 as the primary metric for all three tasks. Compared to MSE, Relative L2 is less influenced by outliers and is more robust. For given n steps 2D predictions $\hat{\mathbf{x}} \in \mathbb{R}^{H \times W \times n}$ or 3D predictions $\hat{\mathbf{x}} \in \mathbb{R}^{H \times W \times C \times n}$ and their corresponding ground truth \mathbf{x} of the same size, the relative L2 can be expressed as:

$$\text{Relative L2} = \frac{\|\mathbf{x} - \hat{\mathbf{x}}\|_2^2}{\|\mathbf{x}\|_2^2}, \quad (19)$$

where $\|\cdot\|_2$ represents the L2 norm.

B Comparison Between DeepLag and Neural ODE-based Methods

DeepLag differs significantly from ODE-based approaches like Neural ODE [4], as highlighted in the comparison Table 7:

While Neural ODE methods explicitly specify ODEs, fluid dynamics is governed by multi-variable PDEs, rendering the ODE formulation inadequate. Moreover, DeepLag is data-driven and does not require explicit ODE

Table 7: Comparison between DeepLag and ODE-based models

Feature	DeepLag	Neural ODE
ODE Specification	Not required	Explicitly specified
Computational Paradigm	Data-driven	Model-driven
Attention Mechanism	Utilizes attention	Typically not utilized
Integration of Lagrangian Dynamics	Integrated	Operates solely in Euler space
Input-Output Mapping	Complex, high-dimensional PDE	Simple, single-variable ODE

specification. Notably, we are the first to employ attention mechanisms for computing Lagrangian dynamics, which closely resemble operators in both deep learning and numerical Lagrangian methods. Additionally, DeepLag integrates both Eulerian and Lagrangian frameworks, whereas ODE-based methods operate solely in the Eulerian space. Finally, DeepLag models the complex mapping of high-dimensional spatiotemporal PDEs, which is significantly more intricate than the simpler processes modeled by single-variable (either temporal or spatial) ODEs.

C More Details about the Benchmarks

C.1 Bounded Navier-Stokes

Here we provide some details about the benchmark Bounded Navier-Stokes. Just as its name implies, the motion of dye is simulated from the Navier-Stokes equation of incompressible fluid. 2000 sequences with spatial resolution of 128×128 are generated for training and 200 new sequences are used for the test. We supplement important details indicating the difficulty of the Bounded Navier-Stokes dataset as follows:

About the Reynolds number The Reynolds number of the dataset is 256. At this Reynolds number, attached vortices dissipate and form a boundary layer separation. The downstream flow field behind the cylinder becomes unsteady, with vortices shedding periodically on both sides of the cylinder’s rear edge, resulting in the well-known phenomenon of *Kármán vortex street* [50]. Additionally, due to the presence of multiple cylinders within the flow field and obstruction from downstream cylinders, more complex flow phenomena than flow around a cylinder occur, challenging the model’s capacity.

Differences of data sequences Our data generation method involves running simulations for over 10^5 steps after setting the initial conditions of the flow field. We then randomly select a starting time step and extract several frames as an example, which are further randomly divided into training and testing sets. Due to the highly unsteady nature of the flow field, the flow patterns observed by the model appear significantly different.

Numerical method used in data generation We utilized the Finite Difference Method (MAC Method) with CIP (Constrained Interpolation Profile) as the Advection Scheme for numerical simulations, implemented by [36]. This high-order interpolation-constrained format effectively reduces numerical dissipation, enhancing the accuracy and reliability of numerical simulations.

C.2 Ocean Current

Some important details related to the Ocean Current benchmark are attached here. Learning ocean current patterns from data and providing long-term forecasts are of great significance for disaster prevention and mitigation, which motivates us to focus on this problem.

The procedures to make this dataset are as follows. First, we downloaded daily sea reanalysis data [5] from 2011 to 2020 provided by the ECMWF and selected five basic variables on the sea surface to construct the dataset, including velocity, salinity, potential temperature, and height above the geoid, which are necessary to identify the ocean state. Then, we crop a 180×300 sub-area on the North Pacific from the global record, corresponding to a $375\text{km} \times 625\text{km}$ region. In total, this dataset consists of 3,653 frames, where the first 3000 frames are used for training and the last 600 frames are used for testing. The training task is to predict the future current of 10 days based on the past 10 days’ observation, after which we performed 30 days of inference with the trained model to examine the long-term stability of DeepLag.

C.3 3D Smoke

To verify our model effectiveness in this complex setting of the high-dimensional tanglesome molecular interaction, we also generate a 3D fluid dataset for the experiment. This benchmark consists of a scenario where

smoke flows under the influence of buoyancy in a three-dimensional bounding box. This process is governed by the incompressible Navier-Stokes equation and the advection equation of fluid. 1000 sequences are generated for training, and 200 new samples are used for testing. Each case is in the resolution of 32^3 .

D Training Curves

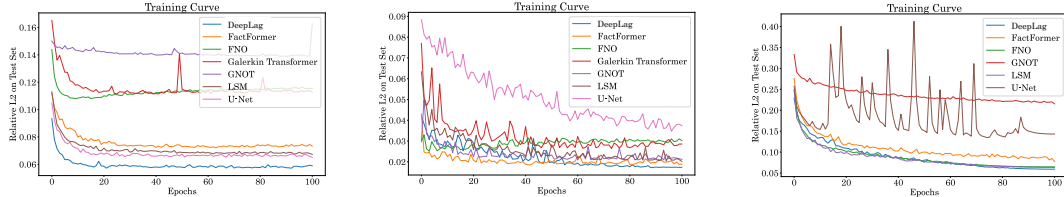


Figure 8: Training curve comparison among all the models on Bounded Navier-Stokes dataset, Ocean Current, and 3D Smoke dataset.

We provide training curves on Bounded Navier-Stokes, Ocean Current and 3D Smoke datasets in Figure 8. We can observe that DeepLag presents favorable training robustness and converges the fastest on the Bounded Navier-Stokes dataset.

E Analysis on the Parameter Count and Performance Difference

In Table 1 in our paper, we present three different datasets with variations in data type, number of variables, number of dimensions, and spatial resolution. Specifically, the 2D fluid and 3D fluid represent *entirely different dynamic systems*, so it is normal for different baselines to perform inconsistently across different benchmarks. In the following results, `patch_size` of all models are set to 1 for fair comparison. For instance, U-Net performs well on datasets with *distinct multiscale attributes* (such as the Bounded Navier-Stokes dataset), while transformer-based methods excel on datasets with *broad practical ranges* (like the Ocean Current dataset) or *high dimensions* (such as the 3D Smoke dataset), where attention mechanisms can effectively model global features. Hence, our model’s ability to handle multiscale and global modeling simultaneously *highlights the challenge of achieving consistent state-of-the-art performance*. Below are the parameter statistics for DeepLag and all baseline models across each benchmark, along with some experiments we conducted to ensure parity in the parameter count for each model.

E.1 Analysis on Bounded Navier-Stokes benchmark

Table 8: Model parameter summary for Bounded Navier-Stokes dataset.

Model	#Parameter
UNet [32]	17,311,489
FNO [21]	4,744,513
Galerkin-Transformer [3]	3,917,600
Vortex [7]	96,321
GNOT [14]	3,736,713
LSM [52]	19,188,033
FactFormer [20]	5,477,185
DeepLag (Ours)	10,895,771

The parameter quantities for each model on the Bounded Navier-Stokes benchmark are shown in Table 8. When attempting to further increase the parameter count of smaller models for fair comparison, we encountered CUDA Out-of-memory errors. Specifically, these errors occurred when we increased the `Dynamic_net_layer` of Vortex from 4 to 50, resulting in a parameter count of 171,761, but encountered CUDA Out of Memory issues.

E.2 Analysis on Ocean Current benchmark

The parameter quantities for each model on the Ocean Current dataset are summarized in Table 9. When attempting to further increase the parameter count of smaller models for fair comparison, we encountered CUDA Out-of-memory errors. Specifically, these errors occurred when we increased the `Dynamic_net_layer` of

Table 9: Model parameter summary for Ocean Current dataset.

Model	#Parameter
UNet [32]	17,314,565
FNO [21]	4,747,589
Galerkin-Transformer [3]	3,941,156
GNOT [14]	993,101
Vortex [7]	96,321
LSM [52]	19,191,109
FactFormer [20]	5,482,821
DeepLag (Ours)	13,782,431

Vortex from 4 to 50, resulting in a parameter count of 171,761, but encountered CUDA Out of Memory issues. Similarly, for GNOT, increasing the `latent_dim` from 64 to 96 resulted in a parameter count of 1,659,179, yet this configuration encountered CUDA Out of Memory errors.

E.3 Analysis on 3D Smoke benchmark

Table 10: Model parameter summary for 3D Smoke dataset.

Model	#Parameter
UNet [32]	51,892,292
FNO [21]	56,651,908
Galerkin-Transformer [3]	28,867,841
GNOT [14]	1,450,768
LSM [52]	25,937,732
FactFormer [20]	1,840,004
DeepLag (Ours)	19,526,827

The parameter quantities for each model on the 3D Smoke dataset are shown in Table 10. When experimenting with increasing the parameter count of certain models for fair comparison, we encountered CUDA Out-of-memory errors. Specifically, these errors occurred when we increased the `latent_dim` of GNOT from 64 to 96, resulting in a parameter count of 1,450,768 for GNOT, which encountered CUDA Out of Memory issues. Similarly, when adjusting the `encoder_transformer_layer` of FactFormer from 3 to 13, the parameter count reached 7,382,084, yet this configuration encountered CUDA Out of Memory errors.

Figure 7 in our paper, along with the provided tables above, illustrate our rigorous comparison and efforts to standardize model parameters for a fair comparison. However, due to excessive GPU memory consumption of intermediate results in some baseline models, we could not conduct direct performance comparisons under matched parameter conditions. The ability of our model to efficiently utilize GPU memory resources is a valuable aspect of practical applications.

F ACC Metric on Ocean Current

Latitude-weighted Anomaly Correlation Coefficient In meteorology, directly calculating the correlation between predictions and ground truth may obtain misleadingly high values because of the seasonal variations. To subtract the climate average from both the forecast and the ground truth, we utilize the Anomaly Correlation Coefficient to verify the forecast and observations. Moreover, since the observation grids are equally spaced in latitude, the size of the different grids is related to the latitude and thus, we calculate the latitude-weighted Anomaly Correlation Coefficient, which can be formalized as:

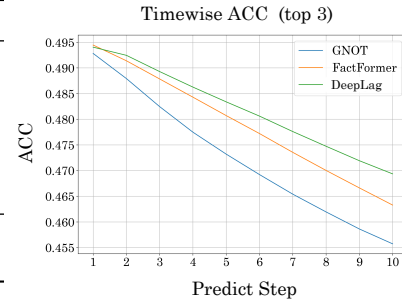
$$\text{ACC}(v, t) = \frac{\sum_{i,j} \text{Lat}(\phi_i) \hat{\mathbf{x}}_{i,j,t}^v \mathbf{x}_{i,j,t}^v}{\sqrt{\sum_{i,j} \text{Lat}(\phi_i) (\hat{\mathbf{x}}_{i,j,t}^v)^2 \times \sum_{i,j} \text{Lat}(\phi_i) (\mathbf{x}_{i,j,t}^v)^2}}, \quad (20)$$

where v represents a certain observed variable, $\hat{\mathbf{x}}_{i,j,t}$ is the prediction of ground truth \mathbf{x} at position i, j and forecast time t . $\mathbf{x}' = \mathbf{x} - \bar{\mathbf{x}}$ represents the difference between \mathbf{x} and the climatology $\bar{\mathbf{x}}$, that is, the long-term mean of observations in the dataset. $\text{Lat}(\phi_i) = N_{\text{Lat}} \times \frac{\cos \phi_i}{\sum_{i'=1}^{N_{\text{Lat}}} \cos \phi_{i'}}$, where $N_{\text{Lat}} = 180$ and ϕ_i is the latitude of the i -th row of output.

ACC result on the Ocean Current benchmark Notably, DeepLag also excels in the ACC metric as shown in Table 11, which can better quantify the model prediction skill. As shown in the timewise ACC curve,

Table 11: ACC results on the Ocean Current dataset and the curve of timewise ACC. Both ACC averaged from 10 prediction steps and ACC of the last prediction frame are recorded. A higher ACC value indicates better performance. Relative promotion is also calculated.

MODEL	AVG. ACC (\uparrow)	LAST. ACC (\uparrow)
U-NET [32]	0.0916	0.0888
FNO [21]	0.0883	0.0853
GALERKIN TRANSFORMER [3]	0.0896	0.0848
GNOT [14]	0.4725	0.4557
LSM [52]	0.2378	0.2305
FACTFORMER [20]	<u>0.4789</u>	<u>0.4633</u>
DEEPLAG (OURS)	0.4820	0.4694
PROMOTION	0.6%	1.3%



DeepLag consistently achieves the highest ACC and holds more significant advantages in long-term prediction. Since ACC is calculated with long-term climate statistics, further improvements become increasingly challenging as it increases, which highlights the value of DeepLag.

G Visual Results for learnable sampling

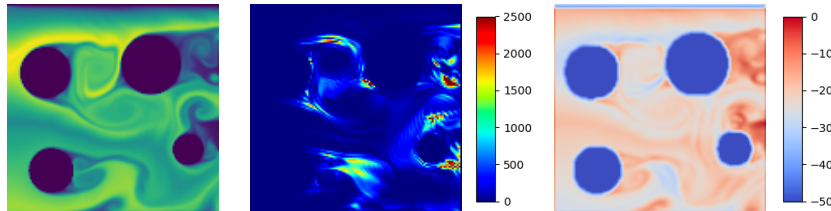


Figure 9: Visualization of the pointwise variance of vorticity (middle) and the sampling probability distribution (right) learned by DeepLag. For a better view, we plot the $\log(S)$ here.

To demonstrate the effectiveness of our learnable probability, we visualize its distribution S with respect to the pointwise variance of vorticity, which is directly proportional to the local complexity of fluid dynamics, in Figure 9. It is evident that our sampling module tends to prioritize regions with higher dynamical complexity, such as the *wake flow* and *Karman vortex* [50] behind the pillar. The showcase in Figure 1 also demonstrates that the tracked particle can well present the dynamics of a certain area. This observation underscores that our design effectively guides the model to track the most crucial particles, enhancing its performance.

H More Showcases

As a supplement to the main text, we provide more showcases here for comparison (Figure 10-15).

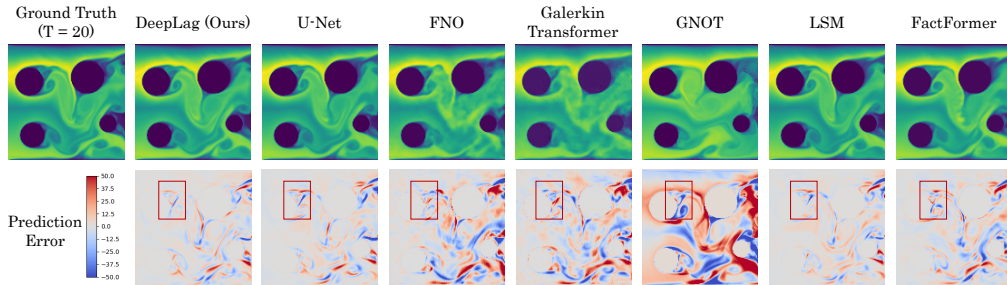


Figure 10: Showcases of the Bounded Navier-Stokes dataset.

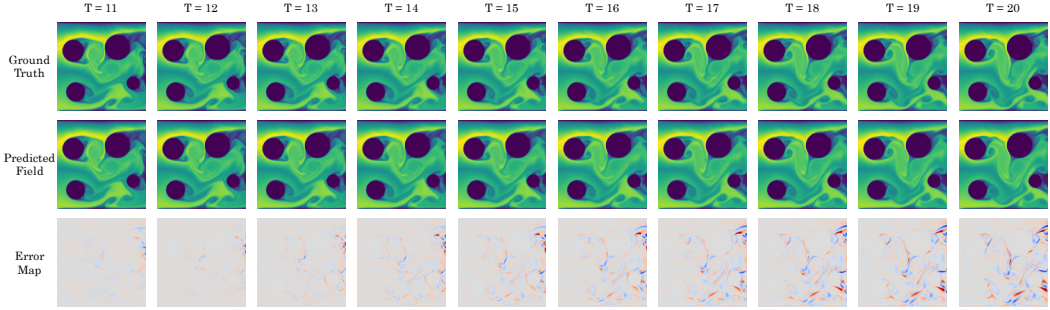


Figure 11: Showcases of DeepLag on the Bounded Navier-Stokes dataset.

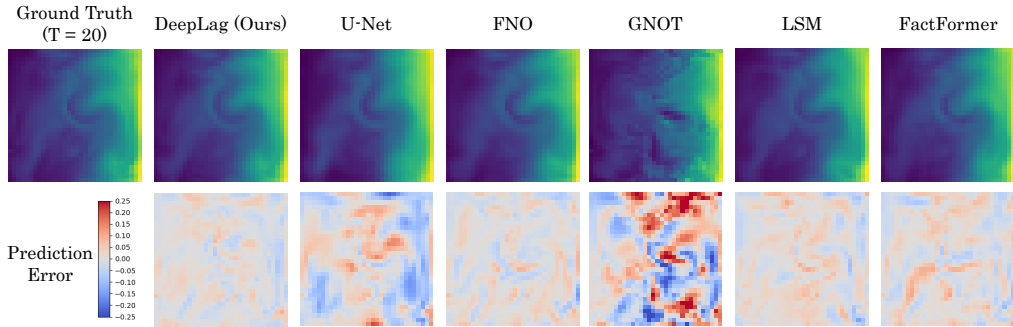


Figure 12: Showcases of the 3D Smoke dataset.

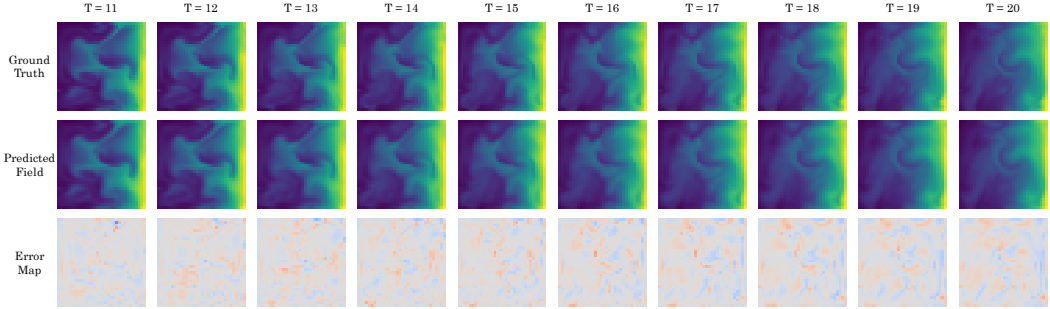


Figure 13: Showcases of DeepLag on the 3D Smoke dataset.

I Result of Long-term Prediction

I.1 Reason for predicting 10 steps

Predicting the last 10 steps from the first 10 steps input is a convention (refer to FNO where $\nu = 1e - 5$, $T = 20$ is the setting, and later several baselines using the NS dataset also followed this setting). We did this to follow the convention and for ease of comparison. Additionally, the Ocean Current dataset has a one-day interval between every two frames, and predicting 10 days ahead is already a long horizon.

I.2 Results of long-term rollout

We conducted experiments for long-term (extrapolation beyond hundreds of frames) predictions. Accurately, we utilize trained 10-frame prediction models to perform 100-frame prediction. Our reason for not directly training a model in an autoregressive paradigm to predict the next 100 frames is due to insufficient memory capacity and the issue of gradient explosion or vanishing. The results are as follows. The best result is bold and the second is underlined. The reason we did not run the 3D Smoke dataset is that it is very challenging to load 110 frames of large 3D data at once, which overwhelms our machine. Extra video results are in supplementary materials, which effectively illustrate the performance and consistency of our model’s predictions.

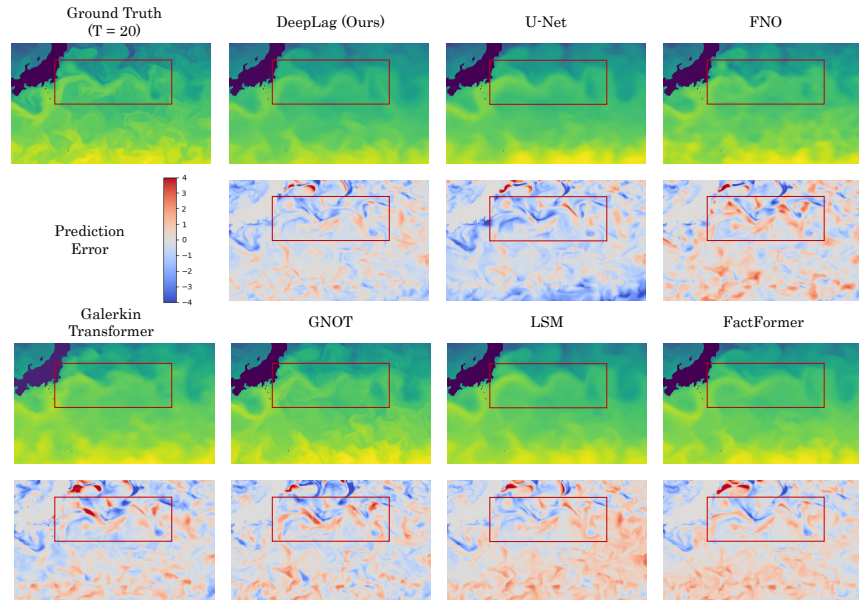


Figure 14: Showcases of the Ocean Current dataset.

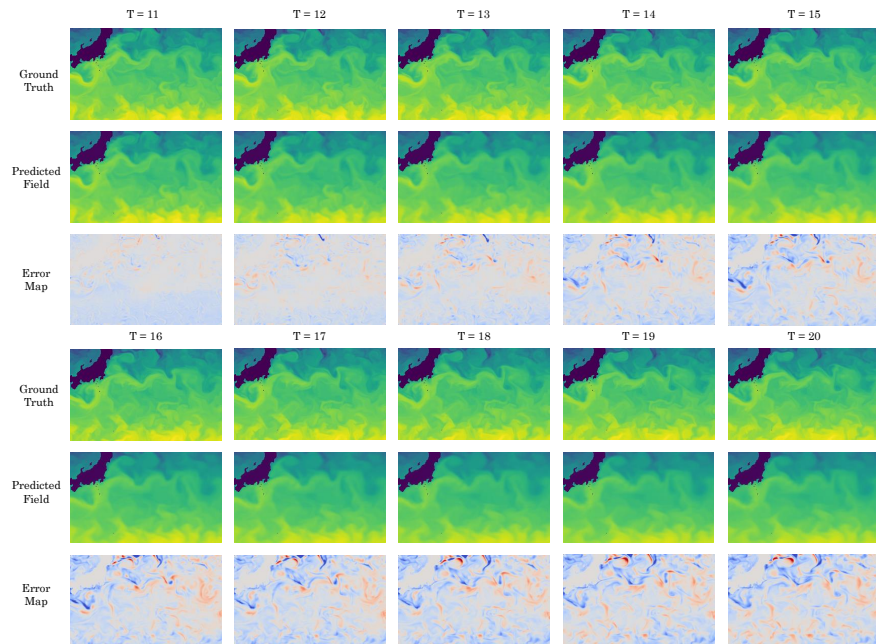


Figure 15: Showcases of DeepLag on the Ocean Current dataset.

I.2.1 Bounded Navier-Stokes

Quantitive results As depicted in Table 12, the DeepLag model still outperforms the strong baselines on the Bounded Navier-Stokes dataset in predicting 100 frames into the future. With a Relative L2 of 0.1493, DeepLag achieves superior performance compared to all baselines. Additionally, the performance trends of all models are visually illustrated in Figure 16 - 20, revealing DeepLag’s ability to maintain lower error growth rates over time, particularly in long-term predictions. This outcome suggests that the Lagrangian particle-based approach adopted by DeepLag effectively captures dynamic information, contributing to its robust forecasting capability in fluid dynamics modeling.

Table 12: Performance comparison for predicting 100 frames on the Bounded Navier-Stokes dataset. Relative L2 is recorded. For clarity, the best result is in bold and the second best is underlined. Promotion represents the relative promotion of our model w.r.t the second best model.

Model	Relative L2 (\downarrow)
U-Net [32]	0.1529
FNO [21]	0.4244
Galerkin-Transformer [3]	0.3010
GNOT [14]	0.2489
LSM [52]	<u>0.1511</u>
FactFormer [20]	0.1691
DeepLag (Ours)	0.1493
promotion	1.2%

Showcases To visually evaluate the predictive capabilities of our models on long-term, we present a showcase of last frame comparisons and time-wise prediction in Figure 16 - 20, illustrating the long-term rollout performance on the Bounded Navier-Stokes dataset. Notably, DeepLag demonstrates remarkable accuracy in capturing complex flow phenomena, accurately predicting the formation and evolution of vortices, particularly the Kármán vortex street behind the upper left pillar. In contrast, U-Net and LSM exhibit moderate success in predicting the central vortex but struggle with accurately reproducing the density distribution of the flow field, as indicated by the error maps. FactFormer, however, shows subpar performance on this benchmark, likely due to its reliance on spatial factorization, which may not effectively handle irregular boundary conditions. These findings underscore the advantages of our Eulerian-Lagrangian co-design approach, which enables simultaneous prediction of dynamics and density, contributing to more accurate and comprehensive fluid modeling and forecasting capabilities. Here are figure showcases of Bounded Navier-Stokes dataset and time-wise prediction with error map:

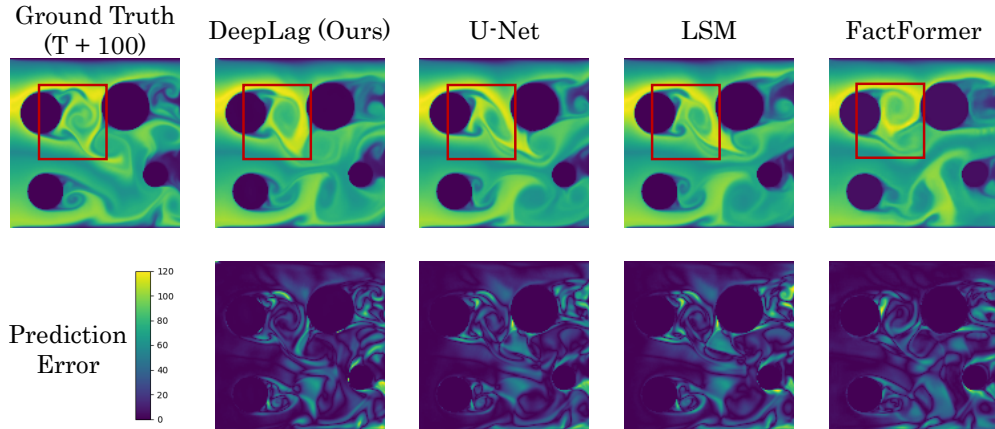


Figure 16: Showcases comparison between the most competitive models of long-term rollout on the Bounded Navier-Stokes benchmark.

I.2.2 Ocean Current

Quantitive results We present a comparison of results for the Ocean Current dataset in Table 13, which includes relative L2, Last frame ACC, and Average ACC metrics. DeepLag maintains its superiority, achieving the lowest relative L2 among all models, with an 8.7% promotion compared to the second-best model. These findings highlight DeepLag’s robust performance in predicting real-world large-scale fluid dynamics, which

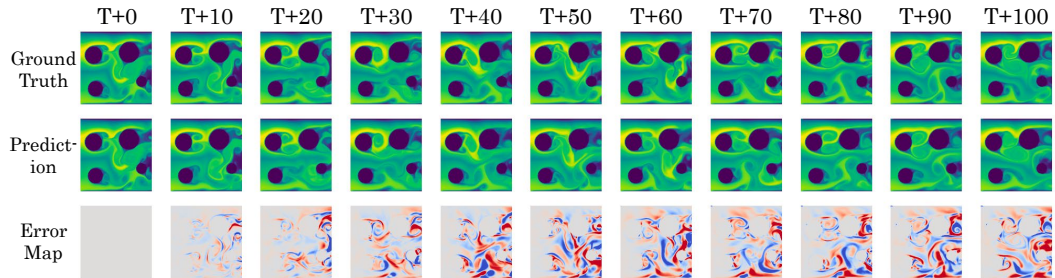


Figure 17: Timewise showcases of DeepLag of long-term rollout on the Bounded Navier-Stokes benchmark.

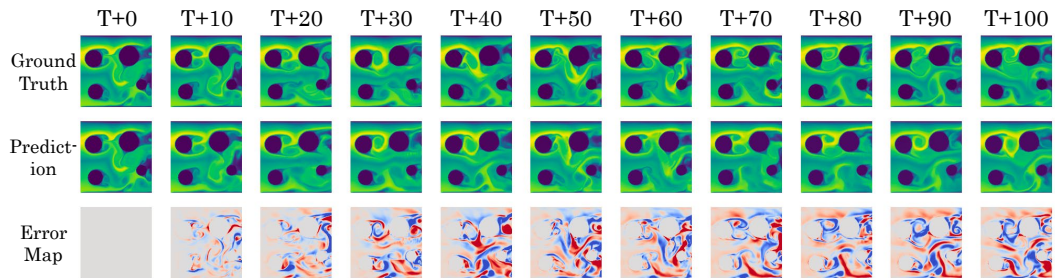


Figure 18: Timewise showcases of FactFormer of the long-term rollout on the Bounded Navier-Stokes benchmark.

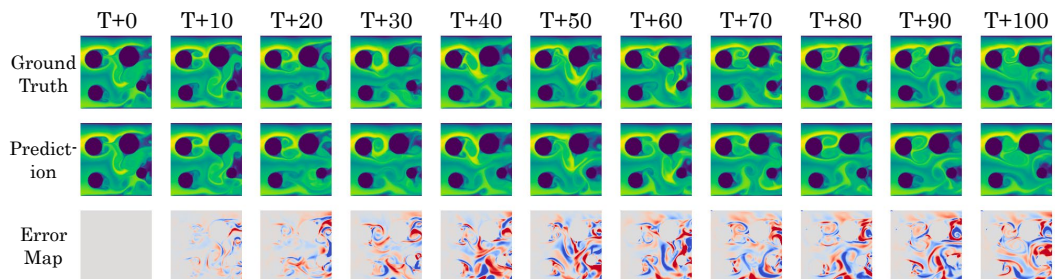


Figure 19: Timewise showcases of LSM of the long-term rollout on the Bounded Navier-Stokes benchmark.

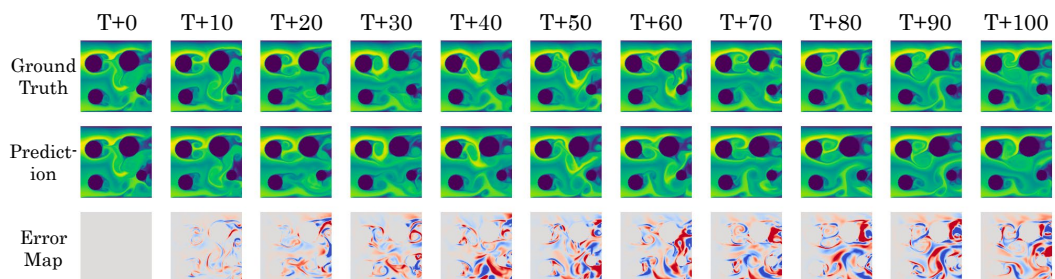


Figure 20: Timewise showcases of U-Net of long-term rollout on the Bounded Navier-Stokes benchmark.

Table 13: Relative L2 for predicting 100 frames, Last frame ACC, and Average ACC

Model	Relative L2 (\downarrow)	Last frame ACC (\uparrow)	Average ACC (\uparrow)
U-Net [32]	0.0764	0.0197	0.0503
FNO [21]	0.1675	0.0041	0.0448
Galerkin-Transformer [3]	NaN	NaN	NaN
GNOT [14]	0.0513	0.173	0.3586
LSM [52]	0.0616	0.0793	0.1650
FactFormer [20]	<u>0.0460</u>	<u>0.2647</u>	<u>0.3864</u>
DeepLag (Ours)	0.0423	0.2890	0.4041
promotion	8.7%	9.2%	4.6%

often exhibit inherent stochasticity. Furthermore, DeepLag outperforms other models in ACC metrics, indicating its superior predictive capability. This is further corroborated by the timewise ACC curve, where DeepLag consistently demonstrates the highest ACC values, particularly in long-term predictions.

Showcases To visually assess the long-term forecasting performance of each model, we showcase the last frame predictions along with their errors, and the time-wise prediction errors for each model in Figure 21 - 25. Visually, our DeepLag predictions closely resemble the Ground Truth compared to other models, demonstrating robust long-term extrapolation capabilities and accurate capture of the *Kuroshio pattern* [37]. It can be observed that FactFormer and LSM exhibit relatively large errors, while GNOT tends to average and loses fine texture details. However, DeepLag does not suffer from these issues.

Here are figure showcases of the Ocean Current dataset:

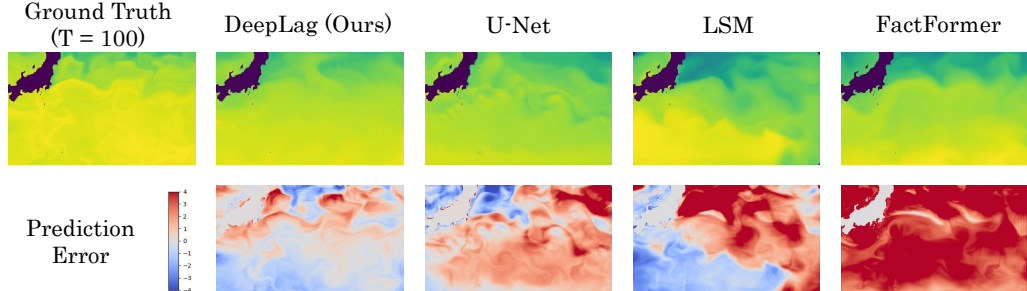


Figure 21: Showcases comparison between the most competitive models of the long-term rollout on the Ocean Current benchmark.

And time-wise prediction with error map:

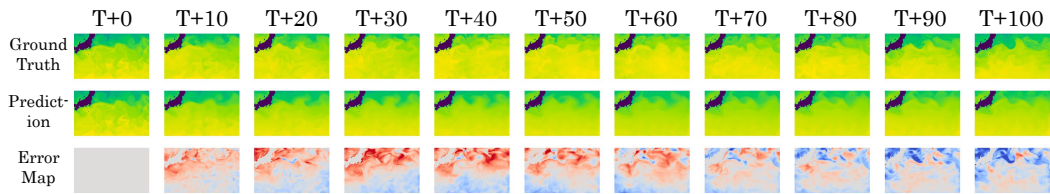


Figure 22: Timewise showcases of DeepLag of the long-term rollout on the Ocean Current benchmark.

I.3 Examination on the turbulent kinetic energy spectrum

In the field of fluid mechanics, simulation results that better adhere to intrinsic physical laws are sometimes more valuable than those with smaller pointwise errors, often reflected in frequency domain analysis. To validate this point and to measure long-term forecasting ability, we introduced a metric on time-averaged turbulent statistics, namely the turbulent kinetic energy spectrum (TKES). Specifically, we computed the MAE and RMSE of TKES for the Bounded Navier-Stokes dataset, which exhibits the most prominent turbulent characteristics, as shown in Table 14, and plotted the line graphs of the error of wave number and TKE, as depicted in Figure 26. It can be observed both numerically and visually that DeepLag consistently outperforms various baselines to different extents.

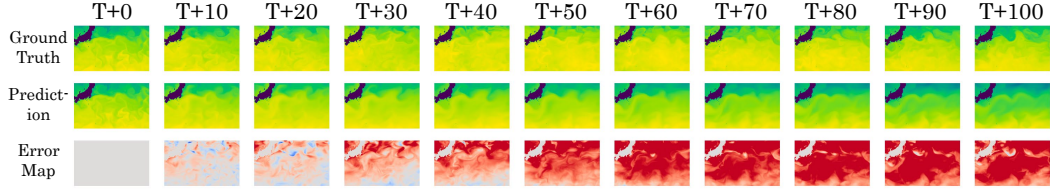


Figure 23: Timewise showcases of FactFormer of the long-term rollout on the Ocean Current benchmark.

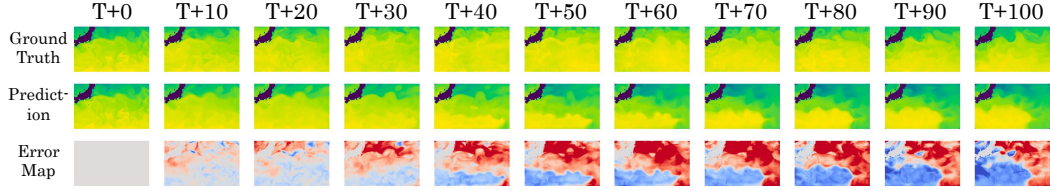


Figure 24: Timewise showcases of LSM of the long-term rollout on the Ocean Current benchmark.

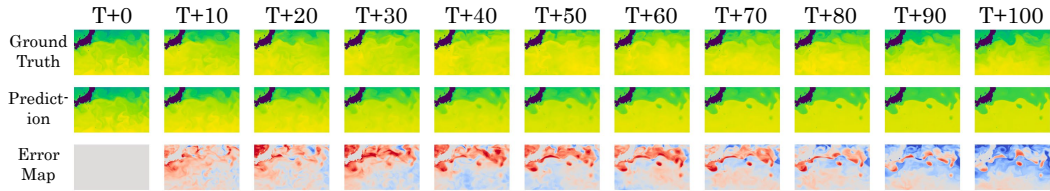


Figure 25: Timewise showcases of GNOT of the long-term rollout on the Bounded Navier-Stokes benchmark.

Table 14: MAE and RMSE of TKES on Bounded Navier-Stokes.

Model	MAE (↓)	RMSE (↓)
U-Net	3.888e+06	3.349e+07
FNO	7.364e+06	7.191e+07
Galerkin-Transformer	5.956e+06	5.950e+07
GNOT	1.210e+07	1.631e+08
LSM	3.403e+06	3.040e+07
FactFormer	4.495e+06	3.968e+07
DeepLag (Ours) promotion	3.052e+06	2.716e+07
	11.5%	11.9%

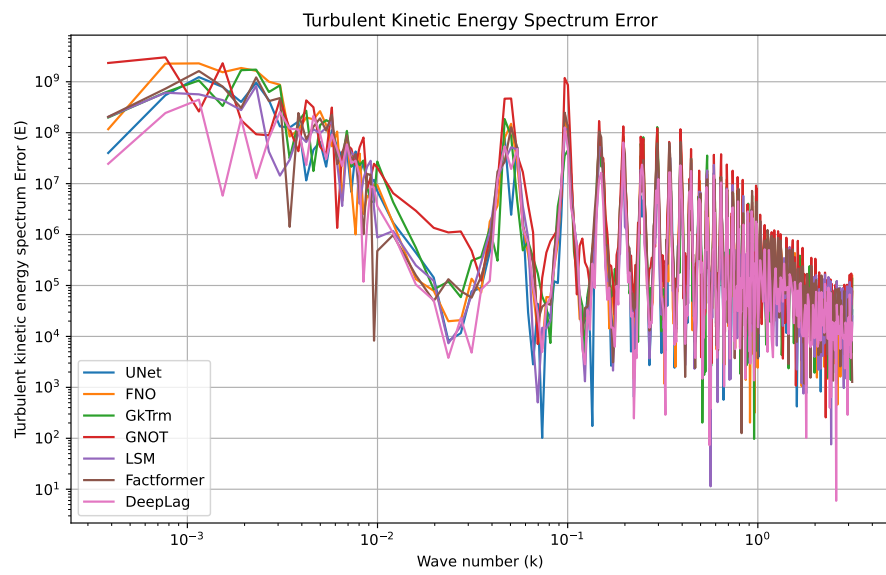


Figure 26: Plot of error of turbulent kinetic energy spectrum w.r.t wave number.